Mineralogical Magazine, October 2017, Vol. 81(5), pp. 1245–1259

OPEN ACCESS

Dissolution kinetics of hydrated calcium aluminates (AFm-Cl) as a function of pH and at room temperature

Nicolas C. M. Marty[1,*], Sylvain Grangeon[1], Catherine Lerouge[1], Fabienne Warmont[2], Olivier Rozenbaum[3], Thibauld Conte[1] and Francis Claret[1]

[1] BRGM, 45060 Orléans Cedex 2, France
[2] ICMN – CNRS - Université d'Orléans, 1b rue de la Férollerie, 45071 Orléans Cedex 2, France
[3] Institut des Sciences de la Terre d'Orléans (ISTO), UMR 6113, 1A, rue de la Férollerie, 45071 Orléans Cedex 2, France

[*Received 1 July 2016; Accepted 19 October 2016; Associate Editor: Claire Corkhill*]

ABSTRACT

The determination of reliable weathering/dissolution rates for cement phases is of fundamental importance for the modelling of the temporal evolution of both radioactive waste repositories and CO_2 geological storage sites (e.g. waste matrix, plug in boreholes). Here, the dissolution kinetics of AFm-Cl (hydrated calcium aluminates containing interlayer Cl) has been studied using flow-through experiments conducted at pH values ranging from 9.2 to 13. Mineralogical (XRD) and chemical (EPMA, TEM) analyses have been performed to determine the evolution of the phases during the dissolution experiments. For pH values between 10 and 13, the dissolution of AFm-Cl is congruent (i.e. Ca/Al ratios close to 2 both for solids and outlet concentrations). In contrast, the precipitation of amorphous Al-phases and possibly amorphous mixed Al/Ca phases is observed at pH 9.2, leading to Ca/Al ratios in the outlet solutions higher than those of the initial solid. Therefore, at pH 9.2, even if Cl^-/OH^- exchange occurs, estimation of dissolution rate from released Cl appears to be the best proxy. Dissolution rates were normalized to the final specific surface areas (ranging from 6.1 to 35.4 $m^2\ g^{-1}$). Dissolution rate appears to be pH-independent and therefore the far-from-equilibrium dissolution rate at room temperature is expressed as: $\log R(\text{mol}\ m^{-2}\ s^{-1}) = -9.23 \pm 0.18$

Keywords: hydrated calcium aluminates, AFm, Friedel's salt, dissolution, kinetics.

Introduction

In most of the designs of deep underground radioactive waste disposal, cementitious materials will be used to build access structures, galleries, vaults and packages for wastes. In such contexts cement materials have essentially a mechanical function (e.g. low permeable barriers that retard radionuclide migration), but can also sorb radionuclides. Indeed, several studies report cationic and anionic sorption on concrete, cement, as well as on pure cement phases (e.g. Aimoz *et al.*, 2012*a*,*b*, 2013; Atkinson and Nickerson, 1988; Baur and Johnson, 2003; Birnin-Yauri and Glasser, 1998; Bonhoure *et al.*, 2006; Cornelis *et al.*, 2012; Gougar *et al.*, 1996; Iwaida *et al.*, 2001; Johnson *et al.*, 2000; Kindness *et al.*, 1994; Miller *et al.*, 2000; Moulin *et al.*, 2000; Pointeau *et al.*, 2008; Pollmann *et al.*, 2006; Segni *et al.*, 2006; Tits *et al.*, 2011; Van Es *et al.*, 2015). Some authors highlight a possible long-term stabilization of the sorbed elements, if phases remain at equilibrium with the surrounding pore water (Cornelis *et al.*, 2012). However, cement materials that will be present *in situ* may be in direct contact with the surrounding rock formation, and thus with rock pore water. The chemical gradient between the cement pore water and the pore water in the host rock will induce mineralogical transformations whose impact must be evaluated in the framework of repository long-

*E-mail: n.marty@brgm.fr
https://doi.org/10.1180/minmag.2016.080.161

term evolution (e.g. Gaucher and Blanc, 2006). Therefore, the stability of cement phases, both from a thermodynamic and kinetic point of view, is a fundamental importance in the determination of radionuclide migration, and more generally, for nuclear safety assessments.

The present study focuses on the stability of hydrated calcium aluminates (AFm), which are phases found in most hydrated cement pastes. AFm are predicted to play a major role in the retention of anionic species (including radionuclides) that might enter in contact with cements, because they possess an anion exchange capacity. This characteristic is due to the fact that the AFm phase belongs to the layered double hydroxide family, i.e. phases built of layers bearing a permanent positive charge and separated from each other by an interlayer space containing water and exchangeable anions compensating for the layer charge (Aimoz *et al.*, 2012*a*; Baquerizo *et al.*, 2015; Birnin-Yauri and Glasser, 1998; Matschei *et al.*, 2007; Moulin *et al.*, 2000; Pollmann *et al.*, 2006; Segni *et al.*, 2006; Van Es *et al.*, 2015).

Here, dissolution experiments were performed with a twofold objective: determination of kinetics law for the dissolution of AFm-Cl (i.e. $Ca_4Al_2Cl_2O_6 : 10H_2O$) and of the evolution of AFm structure during dissolution. The initial material was first carefully characterized using a combination of chemical and physical techniques. Dissolution experiments were then performed in flow-through reactors at room temperature and at various basic conditions (pH 9.2 to 13), so as to be representative of those reported during concrete alteration. Indeed, performance assessment calculations report an evolution of pH from 13.2 to 9 inside concrete due to cement/host interactions (e.g. Marty *et al.*, 2015*a*; Marty *et al.*, 2014) and/or concrete carbonation (e.g. Dauzères *et al.*, 2014; Shi *et al.*, 2016). Alteration products were also carefully examined at the end of experiments.

Materials and methods

Materials

AFm samples

To avoid carbonation processes (e.g. Goñi and Guerrero, 2003), all syntheses were performed in a N_2-filled glove box, using ultra-pure water (resistivity = 18.2 MΩ cm) that was degassed prior to placement in the glove box. Synthesis protocol involved mixing C_3A and $CaCl_2 \cdot 2H_2O$ (1:1 molar ratio) at room temperature, following Balonis and Glasser (2009), and allowing the reaction to run for 15 days, with periodical shaking. After 15 days of maturation, synthesized AFm-Cl were filtered (using a 0.45 µm Millipore HVLP membrane filters) and dried (using a lyophilizer Christ Beta 2-8). Fluids were also retrieved and analysed.

Input solutions

All input solutions used during flow-through experiments were prepared with ultra-pure water (resistivity = 18.2 MΩ cm). Buffering solutions were made up of borax ($Na_2B_4O_7 \cdot 10H_2O$) and NaOH for pH values ranging between 9.2 and 11, and of NaOH and KCl for pH values between 12 and 13. The masses of salts used for the preparation of buffer solutions are reported in Table A1 (Supplementary Tables A1–A6 have been deposited with the Principal Editor of *Mineralogical Magazine* and are available from http://www.minersoc.org/pages/e_journals/dep_mat_mm.html). Note that potassium has been added in solution at pH 12 and 13 so as to be consistent with the conditions of cement pore water.

Analytical procedures

Solid analysis

An electron probe microanalyser (EPMA) was used to determine the composition before, and after, dissolution experiments. Matrix corrections were undertaken with a *ZAF* program (Merlet, 1994).

Powder X-ray diffraction was performed with a Bruker D8 Advance diffractometer, equipped with a Cu anode (λ = 1.5418 Å) and a LynxEye detector. Data were acquired in continuous scan mode, in the 5-80°2θ Cu*K*α interval, with a total counting time of 4 h, and were averaged every 0.02°2θ Cu*K*α. To protect samples from alteration by atmospheric CO_2 during measurement, powders were measured in polyimide capillaries (diameter of 1.6 mm) sealed on both sides by glue.

AFm-Cl were analysed prior and after dissolution experiments using transmission electron microscopy (TEM) and energy dispersive X-ray spectrometry (EDX). The TEM samples were prepared by dispersing the powdered samples in alcohol by ultrasonic treatment. One drop of the suspension was deposited on the carbon membrane and the solvent was evaporated at room temperature. High-resolution transmission electron microscopy images were taken using a CM20 PHILIPS operating at 200 kV and having a line resolution of

1.4 Å. Analysis of selected area diffraction patterns was performed using *CrystBox* (Klinger and Jäger, 2015).

The gas-adsorption experiments using nitrogen as the adsorbent were conducted at 77 K on a Quantachrome Nova 2200e surface area analyser. The specific surface areas (SSA) were calculated using the Brunauer–Emmett–Teller (BET) equation (Brunauer *et al.*, 1938) for relative pressures (P/Po, the ratio of pressure to saturation vapour pressure) ranging from 0.005 to 0.35 and using 15 points. The SSA of the AFm were evaluated prior and after dissolution experiments. Before the measurements, the samples were outgassed during 24 h under vacuum.

Solution analysis

The pH was measured immediately after sampling. The apparatus (a Metrohm electrode connected up to a Mettler Toledo pH meter) was calibrated before each analysis. Collected fluids were then acidified using nitric acid (65%, Merck® Suprapur). Calcium and Al concentrations were measured with an ICP-AES (Horiba-Jobin Yvon® Ultima 2) and an ICP-MS (Thermo® seriX 2), respectively. Ion chromatography was used for Cl analysis (Thermo-Dionex® ICS3000). The detection limits were 1.25 10^{-5}, 1.85 10^{-8} and 1.41 10^{-4} mol L^{-1} for Ca, Al and Cl, respectively.

Flow-through experiments

Experimental apparatus

Dissolution experiments were carried out using flow-through reactors at room temperature (Fig. 1). The total volume of the reactor was ~83 mL. The input buffer solution was circulated at a constant flow rate of ~0.5 mL min^{-1} through the reactors using a peristaltic pump (Watson Marlow®, 205U). The input solution was continuously bubbled with N_2 to avoid any dissolved CO_2. The magnetic stirrer was rotated on an axle in order to avoid any grinding of AFm particles between the bar and the bottom of the reactor (Metz and Ganor, 2001). Experiment labels (AFm-Cl-X, where X stands for the dissolution pH), initial masses, average flow rates and experiment durations are reported in Table 1.

Solution sampling

Outlet solutions of experiments performed at pH ranging from 9.2 to 12 were filtered through a 0.01 µm membrane before being collected in the output bottle (Cellulose nitrate filter, Sartorius®). Experiments performed at pH 13 were filtered using a 0.45 µm membrane (Millipore® HVLP), because cellulose nitrate fibre was observed to be unstable under such pH conditions. The fluid sampling allows monitoring of the solution (pH, Ca, Al and Cl) and flow rates as function of time.

Solid sampling

Solid suspensions were collected and filtered (using a 0.45 µm Millipore® HVLP membrane filters) at the end of the experiments. Masses of recovered materials at the end of experiments are reported in Table 1. The minor loss of material during the procedure is unavoidable. However, collected and calculated masses from solution chemistries are in the same order of magnitude (see Supplementary Tables A1-6, deposited at http://www.minersoc.org/pages/e_journals/dep_mat_mm.html).

Calculation methods

Dissolution rates

The stirred flow-through reactors allows for the control of reaction conditions (i.e. constant pH conditions using a buffer solution as input). The experimental setup is powerful for the measurement of reaction rates at steady state (reached when the outlet concentrations are constant with time). In the case of a congruent reaction, the following expression is verified (Lasaga, 1998):

$$\frac{dN_i}{dt} = 0 = -q(c_i^{out} - c_i^{in}) + \varepsilon_i A R \qquad (1)$$

where N_i is the amount of the atom i (mol), t is the time (s), q is the flow rate (L s^{-1}), $c_i^{out} - c_i^{in}$ is the difference between inlet and outlet concentrations (mol L^{-1}), ε is the stoichiometry of the atom inside AFm-Cl ($\varepsilon_{Ca} = 4$, $\varepsilon_{Al} = 2$ and $\varepsilon_{Cl} = 2$ mol mol^{-1} of AFm), A is the total reactive surface of the mineral (m^2), and R is the dissolution rate (mol m^{-2} s^{-1}).

Therefore equation 1 becomes:

$$R = \frac{q(c_i^{out} - c_i^{in})}{\varepsilon_i A} \qquad (2)$$

In practice, the mineral dissolution rarely attains a steady state. Rather, output concentrations decrease continuously during the alteration process, which may, for example, alter the particles morphology, as observed for illite by Köhler *et al.* (2005). In addition, the amount of altered mineral decreases with time (i.e. dissolution experiment), which may

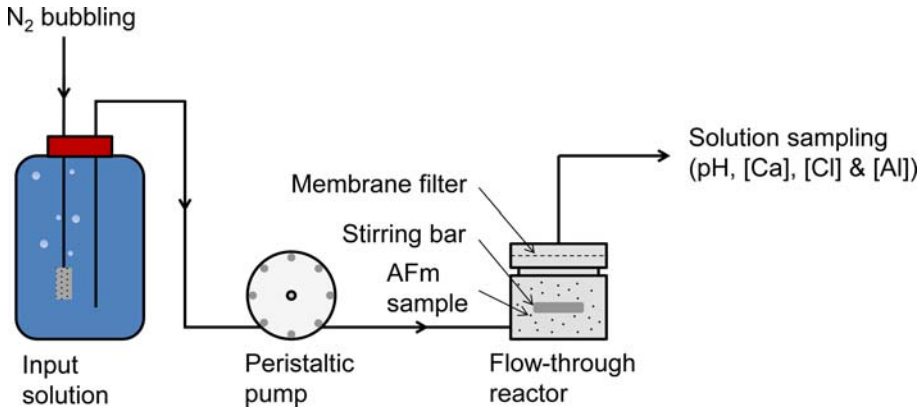

FIG. 1. The experimental apparatus. Modified from Marty *et al.* (2015*c*).

decrease the total reactive surface area (A) and then the amount of elements released in solution. The total reactive surface area is expressed as:

$$A = Sm_t \quad (3)$$

where S is the reactive surface area in (in $m^2\ g^{-1}$, see its estimation in the section Reactive surface area) and m_t is the mass of reacting mineral at the time t (in grams, see its estimation in the section Mass sample evolution).

Reactive surface area

The reactive surface area (S) has been estimated using BET measurements performed on initial and final materials. Following numerous kinetic studies (e.g. Cama *et al.*, 2000; Ganor *et al.*, 1999; Trapote-Barreira *et al.*, 2014), only final BET surfaces have been used to normalize reaction rates. An increase of the BET surface is commonly observed during flow-through experiments. However, as dissolution rates are estimated at the end of experiments, the final BET surface constitutes a suitable proxy. Moreover, it should be noted that reactive surface areas were measured on freeze-dried samples that may contain less interlayer water than when they are in solution (Baquerizo *et al.*, 2015).

Mass sample evolution

Table 1 indicates a significant evolution of the reacting-material masses during dissolution experiments (up to 96 wt.% for the AFm-Cl-11 experiment). Mass variations are therefore taken into account in dissolution-rate calculations:

$$m_t = m_0 - \sum_t V_t \frac{((c_i^{out})_t - (c_i^{in})_t)}{\varepsilon_i} M_{AFm} \quad (4)$$

where m_0 is the initial mass of added AFm (g), M_{AFm} is the molar mass ($g\ mol^{-1}$) of AFm and V is the volume of sampled solution (L).

TABLE 1. Experimental conditions.

Experiment	Average flow rate ($mL\ min^{-1}$)	Input solution	Used material	Initial mass (g)	Duration (h)	Final mass (g)
AFm-Cl-9.2	0.49	A	AFm-Cl(a)	1.2340	27	0.9168
AFm-Cl-10	0.48	B	AFm-Cl(a)	1.1577	47	0.2431
AFm-Cl-11	0.46	C	AFm-Cl(a)	1.3250	51	0.0510
AFm-Cl-12	0.46	D	AFm-Cl(a)	1.2406	47	0.4350
AFm-Cl-13	0.48	E	AFm-Cl(b)	1.0078	46	0.6357

TABLE 2. Compositions (mol mol^{-1} of AFm) of unreacted materials determined from EPMA.

Synthesis	Ca	Al	Cl	Considered structural formula*
AFm-Cl (a)	4.2 ± 0.2	1.9 ± 0.1	1.8 ± 0.0	$Ca_4Al_2Cl_2O_6{:}10H_2O$
AFm-Cl (b)	4.2 ± 0.1	1.9 ± 0.1	1.9 ± 0.1	$Ca_4Al_2Cl_2O_6{:}10H_2O$

*Assuming a temperature of 25°C and assuming the presence of ten water molecules per structural unit (e.g. Rapin *et al.*, 2002; Renaudin *et al.*, 1999).

Calculation of ionic activity products and solution saturation index

Ionic activity products (IAP) and solution saturation index (SI) were calculated from the composition of the fluids retrieved at the end of the synthesizing procedures and from the solutions sampled during dissolution experiments, using *PHREEQC* code (Parkhurst and Appelo, 1999) and the *THERMODDEM* database (Blanc *et al.*, 2012).

Results and discussion

Characterization of the initial material

Solid characterization

So as to obtain enough material for all experiments, two independent batchs of AFm-Cl synthesis have been conducted, following the same protocol. The composition of the obtained solids was similar, as shown in Table 2, both having measured atomic ratios of Ca, Al and Cl in very good agreement with the ideal stoichiometry of a pure AFm-Cl (i.e. Ca/Al = 2, Al/Cl = 1). Refinement of the experimental XRD pattern (Fig. 2) confirms sample purity, as expected from chemical data. The sole presence of the two polytypes of AFm-Cl was necessary to attain a satisfying fit to the data, and almost no change in structure parameters as compared to those provided by Renaudin *et al.* (1999) was needed to reproduce the data. In particular, *c* deviated by < 2% as compared to the model proposed by those authors. Complementary TEM observations of the initial material (Fig. 3) show that crystals have a typical size of 100–1000 nm in the **ab** plane and an automorphic hexagonal shape in the **ab** plane. Because the alteration experiments were expected to reduce the amount of sample available for analysis and thus to possibly exclude the possibility of performing XRD analyses, selected-area electron diffraction (SAED) patterns

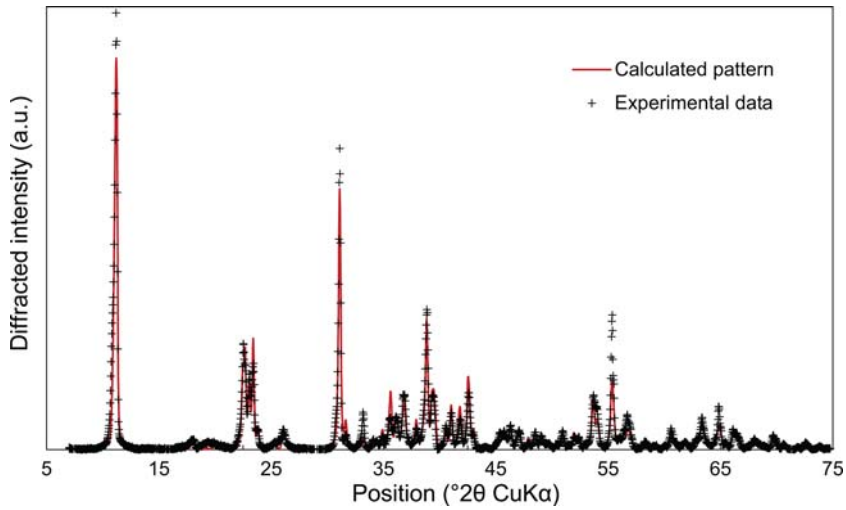

FIG. 2. Experimental AFm-Cl XRD pattern (black crosses) and best fit to the data (solid red line).

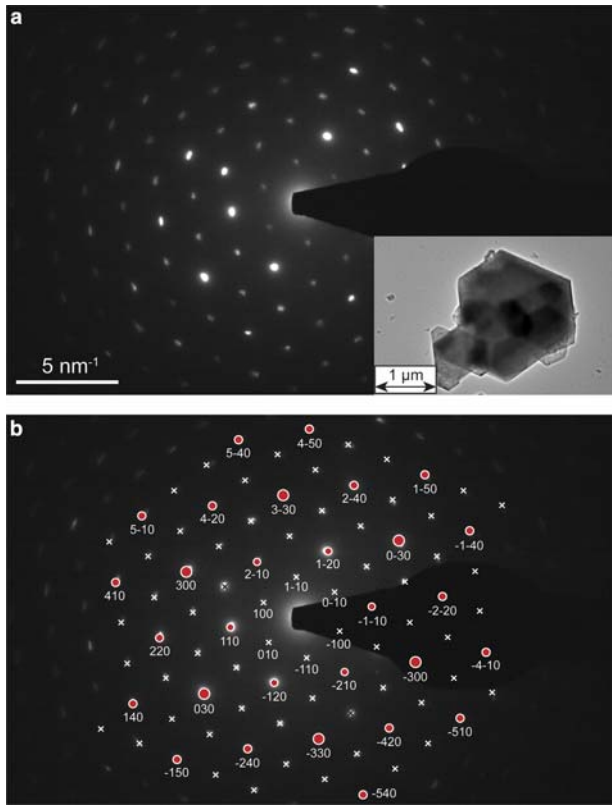

FIG. 3. TEM observations performed on an AFm-Cl sample before dissolution experiments. EDX analyses give a characteristic atomic abundance in agreement with EPMA (i.e. relative Ca:Al:Cl ratio of 1.0:0.5:0.5). (*a*) SAED pattern of the crystal shown in the inset at the bottom right of the image. (*b*) Indexing of the pattern using the structure model from Renaudin *et al*. (1999). Only central and most intense reflections are indexed. The increase in calculated intensity follows the order of crosses to circles of increasing diameter. The fit to the data converged with a standard deviation of experimental-to-calculated *d*-spacing of 0.0015 Å and with the [001] zone axis, in agreement with visual observation of the crystal (inset in (*a*)).

were also collected. In order to facilitate analysis, they were collected perpendicular to the **ab** plane and were found to be typical for AFm-Cl, in agreement with XRD data (fig. 1; Renaudin *et al.*, 1999). EDX analyses were also collected on several independent crystals and were found to be in agreement with EPMA data, with a relative Ca:Al:Cl ratio of 1.0:0.5:0.5.

The specific surface area (SSA), determined from BET analysis, is 6.4 ± 0.1 m^2 g^{-1}, in agreement with literature data (e.g. 10 m^2 g^{-1}, Dai *et al.*, 2009).

Analysis of the synthesis equilibrium solutions

Compositions of fluids retrieved at the end of the synthesis procedures are given in Table 3. The SI of retrieved solutions with respect to portlandite, katoite (C_3AH_6), gibbsite and an amorphous form of $Al(OH)_3$, noted as gibbsite(am), are reported in Table 4. All these potential secondary phases are undersaturated; their precipitation is therefore not expected during synthesis procedures.

The overall aqueous equilibrium of AFm-Cl is expressed as follows:

$$Ca_4Al_2Cl_2O_6{:}10H_2O + 12H^+ = 2Al^{+3} + 4Ca^{+2} + 2Cl^- + 16H_2O$$

Note that experiments are performed in fully water-saturated conditions, and therefore it was considered that one mole of AFm-Cl contains 10 moles of water. According to this reaction, the average IAP calculated after the synthesis

TABLE 3. Compositions of retrieved fluids during synthesis procedures.

Synthesis	pH	Cl (mol L^{-1})	Al (mol L^{-1})	Ca (mol L^{-1})
AFm-Cl (a)	12.08	$8.46\ 10^{-02}$	$6.93\ 10^{-06}$	$5.86\ 10^{-02}$
AFm-Cl (b)	12.11	$1.07\ 10^{-01}$	$9.04\ 10^{-06}$	$6.62\ 10^{-02}$

TABLE 4. Saturation indexes (SI) of retrieved fluids during synthesis procedures.

Synthesis	$SI_{Portlandite}$	$SI_{Gibbsite(am)}$	$SI_{Gibbsite}$	$SI_{Katoite}$
AFm-Cl (a)	–0.38	–5.08	–2.24	–2.03
AFm-Cl (b)	–0.29	–5.00	–2.16	–1.59

procedures is log IAP = 74.50 ± 0.44 at 25°C. The error on the proposed log IAP has been established from the standard error obtained from the two syntheses of AFm-Cl. The value is in agreement with the thermodynamic constant referenced in *THERMODDEM* (i.e. log K = 74.95). These IAP calculations indicate that synthesized materials are close to a thermodynamic equilibrium. The chemistry of the solutions retrieved is therefore consistent with the formation of pure AFm-Cl.

AFm dissolution kinetics

Fluid-chemistry evolutions

Inlet/outlet pH measurements, as well as Ca, Al and Cl concentrations during flow-through experiments, are given in the supplementary data (Tables A1–6, deposited). The evolution of concentrations over time obtained during the AFm-Cl-9.2 experiment (dissolution at pH 9.2) indicate that a steady state was not reached for both Cl and Ca outlet concentrations. In contrast, a steady state may

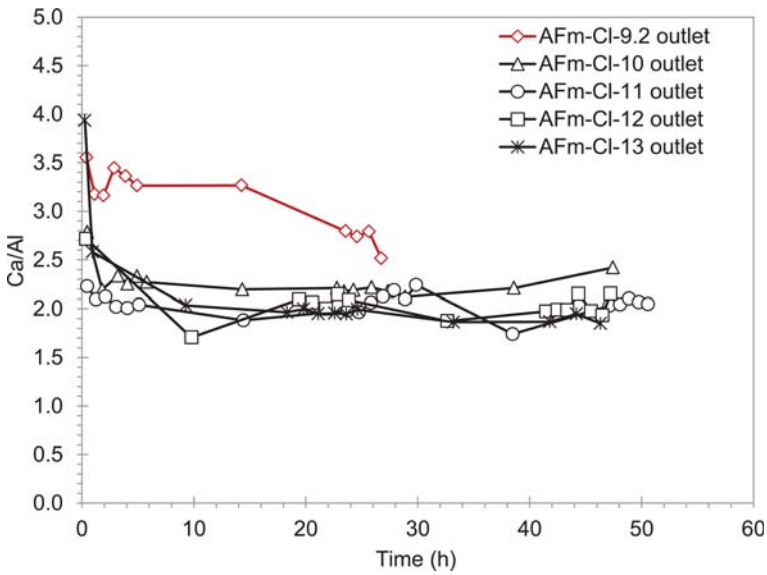

FIG. 4. Ca/Al ratios calculated from outlet concentrations monitored during flow-through experiments.

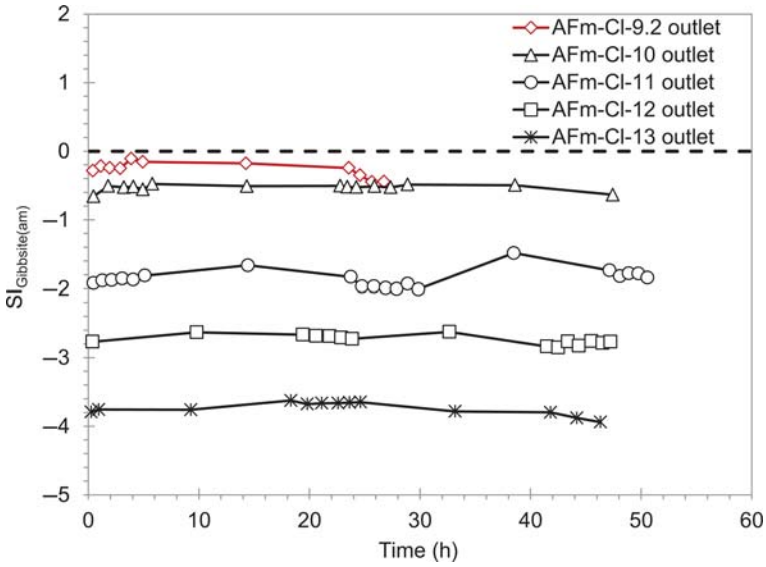

FIG. 5. Saturation indexes of gibbsite(am) during dissolution experiments. Calculations performed with *PHREEQC* (Parkhurst and Appelo, 1999) using the *THERMODDEM* database (Blanc *et al*., 2012).

be assumed for Cl outlet concentration; therefore Cl constitutes a best proxy in the estimation of dissolution rate. Similarly, in the AFm-Cl-10 experiment (pH = 10), an approximate steady state is observed after 20 h of dissolution experiment whatever the considered element. Two distinct steady states are distinguished for the experiment AFm-Cl-11: a first one between 25 and 30 h (pH ~11.7) and a second one after 45 h (pH ~10.8). At pH 12 and 13 (i.e. AFm-Cl-12 and AFm-Cl-13 experiments), Ca, Cl and Al outlet concentrations appear to be relatively constant over time.

Output pH values were always higher than input values for pH ranging from 9.2 to 12. Conversely, in the experiment performed at pH 13, output pH is lower than in the input solution. Such an evolution can be explained by pH buffering by the AFm itself, as its equilibrium pH was measured during synthesis to be ~12.1 (Table 3).

In experiments performed at pH 12 and 13, high Cl concentrations were observed, as a result of the presence of KCl in input solutions (Table A1, deposited). Chemical analyses performed on inlet solutions indicate that Ca concentrations were always below the detection limit (i.e. 1.25 10^{-5} mol L^{-1}). In contrast, the weak presence of Al in inlet solutions was sometimes observed (see supplementary data, deposited).

The evolution of Ca/Al ratios with time in the outlet solution are reported in Fig. 4. This ratio is close to 2 for experiments performed at pH ranging from 10 to 13, as expected for congruent dissolution of AFm-Cl samples (Table 2). In contrast, at pH 9.2, Ca/Al remained significantly > 2 during the whole alteration experiment, with values of 3.5–2.5. Calculation of the SI of the phases of interest for the present study demonstrates that amorphous $Al(OH)_3$ is close to equilibrium (Fig. 5) in this experiment. Therefore, in such conditions, the formation of amorphous $Al(OH)_3$ cannot be ruled out because it would decrease outlet Al concentrations and therefore lead to the observed high Ca/Al ratios (see Fig. 4). Many authors (e.g. Gardner,

TABLE 5. Compositions (mol mol^{-1} of AFm) determined from EPMA at the end of the dissolution experiments.

Experiment	Ca	Al	Cl
AFm-Cl-9.2	4.0 ± 0.1	2.0 ± 0.1	1.4 ± 0.1
AFm-Cl-10	4.1 ± 0.1	1.9 ± 0.1	1.1 ± 0.1
AFm-Cl-11	3.9 ± 0.2	2.1 ± 0.1	1.0 ± 0.3
AFm-Cl-12	4.1 ± 0.2	1.9 ± 0.1	1.7 ± 0.1
AFm-Cl-13	4.1 ± 0.1	1.9 ± 0.1	1.3 ± 0.1

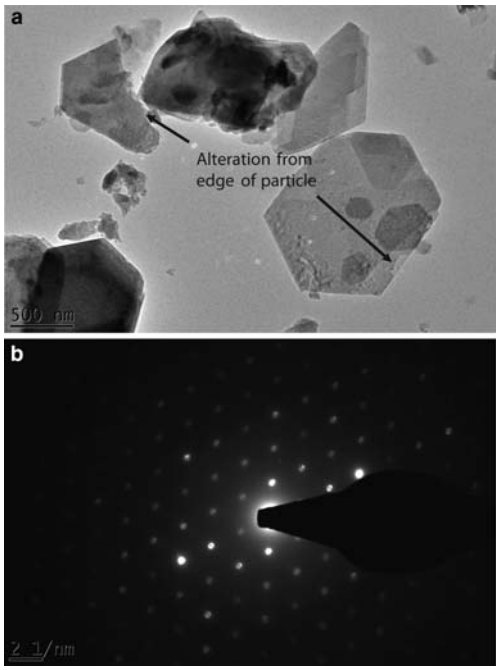

FIG. 6. TEM observations performed on AFm samples after dissolution experiments at pH 12. EDX analyses give a characteristic atomic abundance in agreement with EPMA analyses (i.e. relative Ca:Al:Cl ratio of 1.1:0.5:0.4). (*a*) Electron micrograph showing the alteration of AFm particles. (*b*) Electron-diffraction pattern.

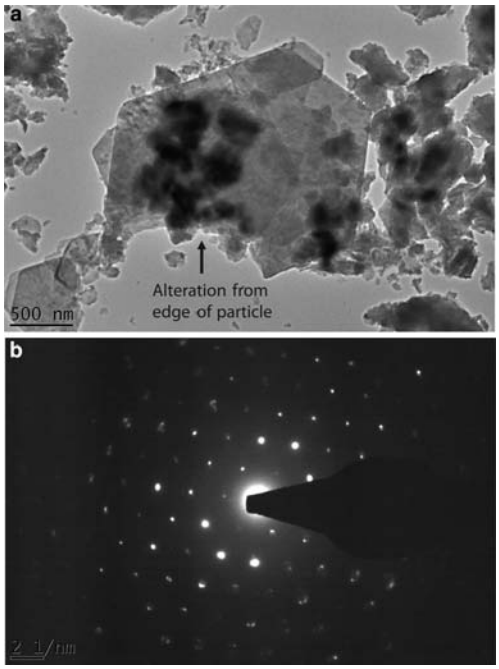

FIG. 7. TEM observations performed on AFm samples after dissolution experiments at pH 9.2. EDX analyses give a characteristic atomic abundance in agreement with EPMA analyses (i.e. relative Ca:Al:Cl ratio of 1:1.5:0.4). (*a*) Electron micrograph showing the alteration of AFm particles. (*b*) Electron-diffraction pattern.

1970; Hem and Roberson, 1967; Hsu, 1966) suggest that amorphous $Al(OH)_3$ precipitates initially from solution and then evolves into a crystalline form (gibbsite) upon ageing. This latter form is more stable from a thermodynamic point of view but is unlikely in our experimental conditions, because of room temperature and low duration of the experiment (27–51 h).

Mineralogical evolution

Data from EPMA collected on solid remaining at the end of the dissolution experiments are reported in Table 5. Final Ca/Al ratios are ≈2 and therefore are fully consistent with solution Ca/Al ratios calculated at pH ranging from 10 to 13. In the experiment conducted at pH 9.2, the average composition of the solid was not found to be enriched in Al, even if high Ca/Al ratios were measured in outlet solutions (Fig. 4). This can be explained straightforwardly because a mass balance calculation from the outlet solution chemistries predicts a composition of the remaining solid close to that of the initial solid (i.e. Ca = 3.9, Al = 2.1 and Cl = 1.5 mol mol^{-1} of AFm). Therefore, Al enrichment of the solid cannot be distinguished on bulk analysis because it is within the range of EPMA uncertainty. In addition, if Al-rich phases were to be formed, they may have been missed as only ten independent analytical points could be collected, owing to the low amount of solid available for this analysis.

In order to understand better the alteration mechanisms at the crystal scale, TEM was employed. As exemplified here with the sample subjected to alteration at pH 12, when alteration pH ranged between 10 and 13, EDX was consistent with EMPA data reported in Table 5 (i.e. relative Ca:Al:Cl ratio of 1.1:0.5:0.4) and SAED patterns were typical for AFm, with a pattern identical to that of the initial material. The presence of numerous rounded and broken particles as well as an alteration process of the particles from edge surface areas (ESA) were identified (Fig. 6). The whole AFm surface appears to be reactive, and

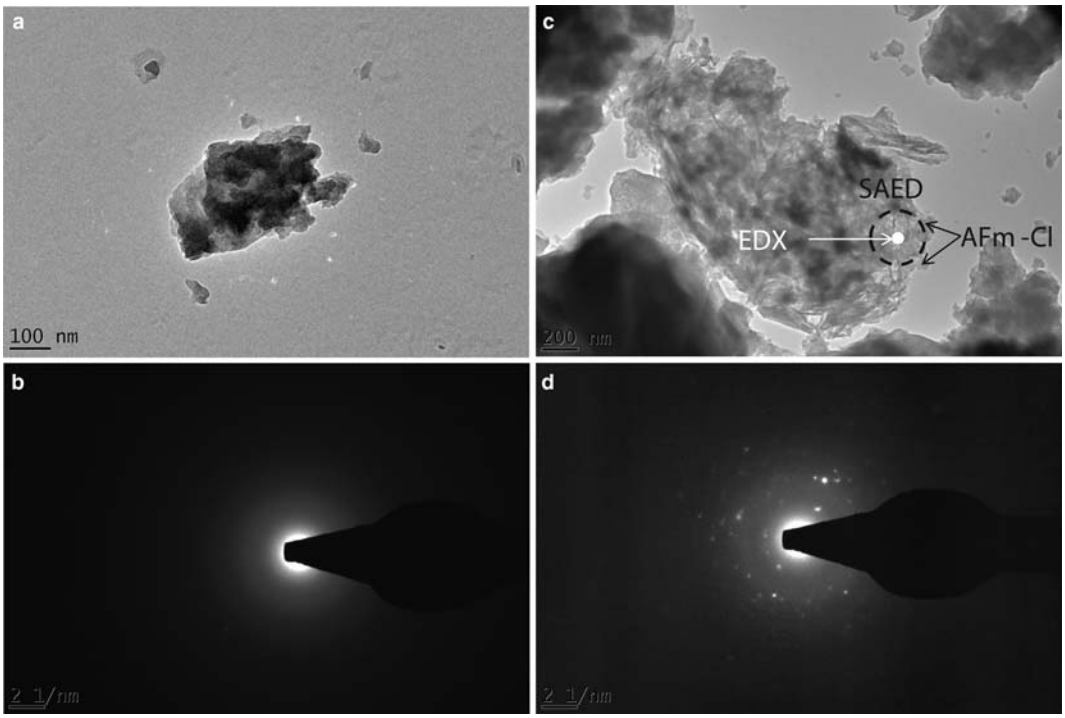

FIG. 8. TEM analyses indicating the secondary-phase formations during the AFm-Cl-9.2 experiment. (*a*) Electron micrograph showing the formation of an Al-rich phase. EDX analyses give a relative Ca:Al:Cl ratio of 0.5:1.4:0.1. (*b*) Electron-diffraction pattern showing the amorphous nature of the Al-rich phase. (*c*) Electron micrograph showing a foil-like morphology. Dotted circle marks the area analysed by SAED in which the presence of AFm-Cl cannot be avoided (arrows). Full white circle indicates the area analysed by EDX. EDX analyses give a relative Ca:Al:Cl ratio of 1.0:1.0:0.0. (*d*) Electron-diffraction pattern showing the amorphous nature of the foil-like morphology, as all diffraction features could successfully be attributed to the AFm matrix.

therefore, the specific surface area (i.e. BET surface area) is assumed to play a role in the dissolution process. No secondary mineral precipitation was observed when alteration pH ranged between 10 and 13.

Analysis of the solid resulting from alteration at pH 9.2 was more complex. First, TEM analyses showed the presence of numerous rounded and broken particles with, again, the regular presence of a dissolution process from ESA (see Fig. 7). In these particles, SAED patterns as well as EDX analyses (relative Ca:Al:Cl ratio of 1.1:0.5:0.4) were typical for AFm (Fig. 3 and Fig. 7). Formation of gibbsite(am), that is a pure $Al(OH)_3$ phase, predicted by geochemical calculations has not been confirmed by TEM observations. However, two types of Al-rich particles were identified. The first type had characteristic relative Ca:Al:Cl ratios of 0.5:1.4:0.1 (Fig. 8*a*), and had a SAED pattern typical for an amorphous phase (Fig. 8*b*). The second type had a foil-like morphology (Fig. 8*c*), did not contain Cl, and had a Ca/Al ratio of 1. In the SAED pattern, all reciprocal lattice points that could be observed resulted from the presence in the background of AFm-Cl (Fig. 8*d*) and thus this second type of Al-rich particle is also amorphous. Note that the fact that SAED showed the presence of AFm-Cl whereas EDX data were incompatible with the presence of an AFm background is simply due to the fact that the size of the areas analysed with the two methods vary: SAED can only be acquired on a circle having a diameter of ~300 nm, whereas EDX analysis can be much more focused (Fig. 8*c*).

Overall, although the present analyses could not confirm the presence of pure amorphous $Al(OH)_3$, the presence of amorphous phases being enriched in Al was evident, which is consistent with

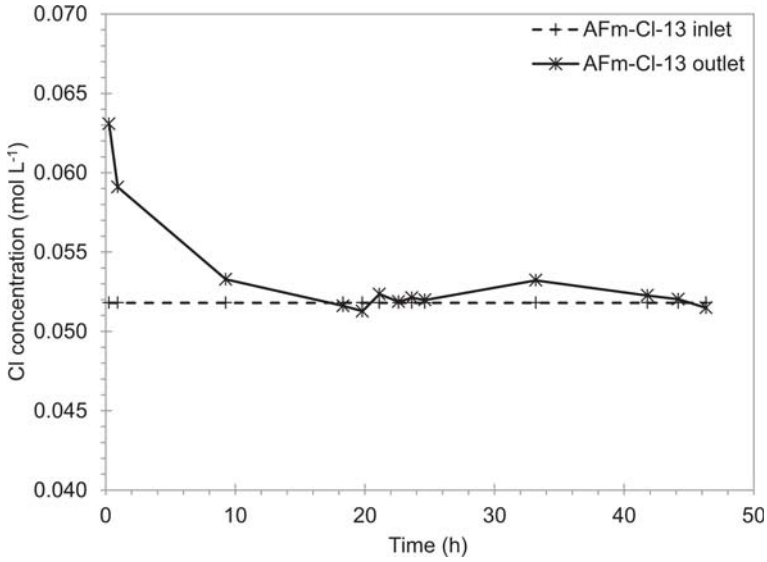

FIG. 9. Evolutions of Cl concentrations during AFm-Cl-13 experiment.

chemical data (Fig. 4). The coherency with thermodynamic predictions cannot be further discussed because such phases are not documented in the considered database.

Exchange reactions

The unreacted AFm-Cl was a pure phase having a Cl content of 2 mol mol^{-1} of AFm (Table 2). Both EPMA and TEM-EDX analyses point to a systematic decrease of the Cl content after alteration experiments (Table 5), while Ca/Al ratio and SAED patterns remained similar for all experiments but pH 9.2, meaning that the AFm layer structure, and thus layer charge, was preserved. Because the main anion in all input solutions was OH^- (Table A1, deposited), the loss of Cl^- certainly reflects the exchange of interlayer Cl^- by interlayer OH^-. Geochemical calculations also indicate the possible exchange of Cl^- by $B(OH)_4^-$ (resulting from the buffering solution) for experiments performed at pH from 9.2 to 11 (i.e. using borate, see Table A1, deposited). Boron uptake by AFm has been studied by Qiu *et al.* (2015). These authors indicate that the affinity of OH^- for the AFm is stronger than that of $B(OH)_4^-$. Therefore, the amount of $B(OH)_4^-$ in the AFm interlayer is probably low (if any) in our experiments. Figure 9 indicates that the exchange process, characterized by an increase of outlet Cl concentrations, occurs in the early stage of dissolution experiments.

Dissolution rates as a function of pH at room temperature

At pH ranging from 10 to 13, Ca/Al ratios of both solids and solutions indicate a congruent dissolution process; dissolution rates can be therefore calculated directly from outlet Ca and Al concentrations. In contrast, solution chemistries for the experiment performed at pH 9.2 indicates non-congruence (Ca/Al ratio > 2). In such conditions, geochemical calculations and TEM observations indicate the precipitation of amorphous Al-rich and mixed Al/Ca phases. Such formations explain the absence of a steady state for Ca and Al outlet concentrations and raises a question about the validity of equation 2 for this experiment. Consequently, estimated rates from released Ca and Al at pH 9.2 are subject to significant and unquantifiable uncertainties and are probably underestimated. In addition, estimating reaction rates from outlet Cl is not possible, because this ion is subject to exchange reactions in the early stages of dissolution experiments (Fig. 9). These limitations can be circumvented by considering final AFm-Cl compositions reported in Table 5 as well as the mass evolution estimated from released Ca. Outlet Cl concentrations can then be used to calculate dissolution rates. Unfortunately, such calculations are impossible at pH 12 and 13 due to the high amount of Cl in input solutions (see Table A1, deposited).

TABLE 6. Calculated dissolution rates as function of pH.

Experiment	pH_{out}	Flow rate (mL min^{-1})	Final BET (m^2 g^{-1})	R_{Ca} (mol m^{-2} s^{-1})	R_{Al} (mol m^{-2} s^{-1})	R_{Cl} (mol m^{-2} s^{-1})	$SI_{AFm\text{-}Cl}$
AFm-Cl-9.2	9.27 ± 0.06	0.48 ± 0.01	9.4 ± 0.2	2.37 (±0.25) 10^{-10}	1.28 (±0.12) 10^{-10}	4.25 (±0.48) 10^{-10}	–17.36
AFm-Cl-10	10.02 ± 0.03	0.47 ± 0.02	13.7 ± 0.7	8.43 (±0.67) 10^{-10}	7.08 (±0.45) 10^{-10}	1.23 (±0.06) 10^{-09}	–10.72
AFm-Cl-11a	11.71 ± 0.02	0.42 ± 0.01	35.4 ± 7.2	6.59 (±0.50) 10^{-10}	6.38 (±0.38) 10^{-10}	8.04 (±0.90) 10^{-10}	–2.64
AFm-Cl-11b	10.84 ± 0.10	0.46 ± 0.01	35.4 ± 7.2	2.92 (±1.00) 10^{-10}	3.44 (±1.32) 10^{-10}	3.38 (±1.88) 10^{-10}	–11.12
AFm-Cl-12	12.02 ± 0.08	0.46 ± 0.01	7.1 ± 0.2	7.70 (±1.21) 10^{-10}	7.93 (±1.18) 10^{-10}	—*	–1.68
AFm-Cl-13	12.78 ± 0.03	0.48 ± 0.00	6.1 ± 0.1	5.20 (±1.27) 10^{-10}	5.37 (±1.19) 10^{-10}	—*	–1.12

R_{Ca}, R_{Al} and R_{Cl} stand for dissolution rates estimated from outlet Ca, Al and Cl concentrations, respectively. SI_{AFM-Cl} refers to the saturation index of the solution with respect to the AFm-Cl.
*Calculation is impossible due to the high amount of Cl in the input solution.

Specific surface areas obtained on the final solids, calculated dissolution rates and saturation of outlet solutions with respect to AFm are given in Table 6. As indicated by saturation indexes, dissolution experiments conducted at pH 9.2–12 have been performed in far-from-equilibrium conditions and the dissolution kinetics thus are independent of the saturation ratio (e.g. Cama *et al.*, 1999; Marty *et al.*, 2015*b*). In contrast, at pH 13, a deviation-from-equilibrium effect on dissolution rate may occur (SI = –1.12). Therefore, the measured dissolution rate during the AFm-Cl-13 experiment could be slightly underestimated. Note that the amount of the retrieved material at the end of the AFm-Cl-11 experiment is weak (i.e. 0.05 g, see Table 1); therefore, the uncertainty on the BET measurement is probably higher than the one reported in Table 6 (i.e. 35.4 ± 7.2 m^2 g^{-1}).

The BET surface areas used for the normalization do not necessarily correspond to reactive surface areas, i.e. not really involved in the dissolution process. For example, several authors report a clay dissolution from edge surface areas (ESA) in basic conditions (e.g. Marty *et al.*, 2011) with measured ESA significantly lower than BET areas (e.g. ESA = 11.2 m^2 g^{-1} and BET = 104 m^2 g^{-1} for a synthetic montmorillonite). Nevertheless, in our study TEM observations indicate an isotropic particle alteration (including ESA) and surfaces have been normalized according to BET (Fig. 10). On the basis of this assumption, no significant effect of pH on dissolution rates can be observed.

Under our experimental conditions, dissolution rates appear to be pH-independent and therefore, an average dissolution rate has been calculated over the range of investigated pH. The far-from-equilibrium dissolution kinetics at room temperature is expressed as: $\log R(\text{mol m}^{-2}\text{ s}^{-1}) = -9.23 \pm 0.18$

Conclusion

AFm-Cl has been synthesized successfully and the phase alteration studied with flow-through experiments performed at room temperature and various pH conditions (i.e. $9.2 < pH < 13$). Flow-through experiments combined with mineralogical (XRD) and compositional (EPMA, TEM, ICP-AES, pH measurements) analyses make up an excellent tool for evaluating AFm alteration. Efficiency/safety evaluations of many systems, including the long-term geochemical evolution of host rocks considered for high-level nuclear waste repositories or

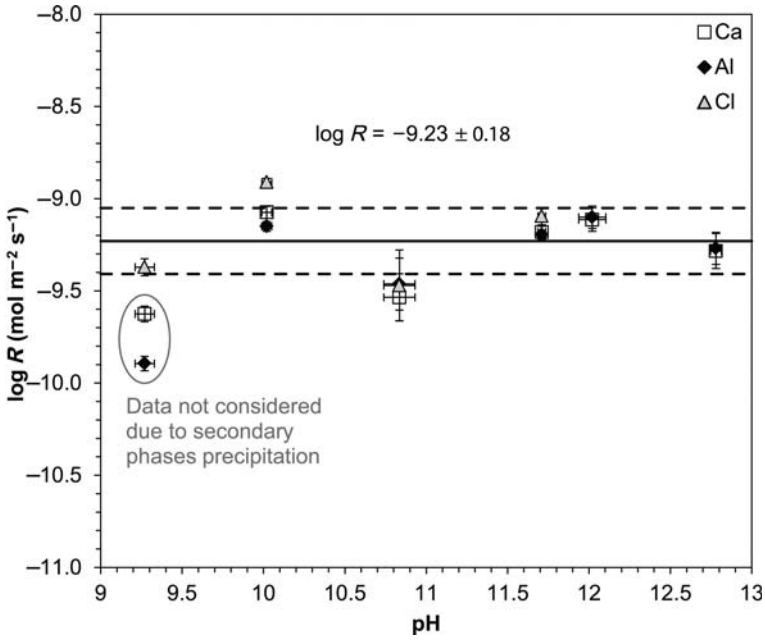

FIG. 10. AFm dissolution rates as function of pH at room temperature (mol m^{-2} s^{-1}).

the integrity of cap-rocks for CO_2 geological sequestration are usually performed using reactive transport modelling. Among others, the prediction of natural and engineered barriers evolution upon geochemical gradients is of paramount importance (Bildstein and Claret, 2015). The modelled mineralogical transformation pathways can be affected both by kinetics reaction rates and mesh refinement (Marty *et al.*, 2009). Therefore being able to implement an accurate kinetic reaction rate in the reactive transport calculation, like the one described in this paper, will form a sound basis in time-barrier evolution. More specifically, the following conclusions can be drawn: there is a congruent dissolution process for pH ranging from 10 to 13; there is a formation of amorphous Al-rich phases as well as amorphous Ca/Al-mixed phases for the experiment performed at pH 9.2; no significant effect of pH on dissolution rate can be drawn.

Acknowledgements

The research leading to these results has received funding from the European Union's European Atomic Energy Community's (Euratom) Horizon 2020 Programme (NFRP-2014/2015) under grant agreement, 662147 – Cebama. S.G. acknowledges partial funding by the ANR (grant ANR-14-CE01-0006).

References

Aimoz, L., Kulik, D.A., Wieland, E., Curti, E., Lothenbach, B. and Mäder, U. (2012*a*) Thermodynamics of AFm-(I_2, SO_4) solid solution and of its end-members in aqueous media. *Applied Geochemistry*, **27**, 2117–2129.

Aimoz, L., Wieland, E., Taviot-Gueho, C., Dahn, R., Vespa, M. and Churakov, S.V. (2012*b*) Structural insight into iodide uptake by AFm phases. *Environmental Science & Technology*, **46**, 3874–3881.

Aimoz, L., Wieland, E., Kulik, D.A., Lothenbach, B., Glaus, M.A. and Curti, E. (2013) Characterization and solubility determination of the solid-solution between AFm-I_2 and AFm-SO_4. Pp. 57–65 in: *Cement-Based Materials for Nuclear Waste Storage* (F. Bart, C. Cau-di-Coumes, F. Frizon and S. Lorente, editors). Springer New York, New York.

Atkinson, A. and Nickerson, A.K. (1988) Diffusion and sorption of cesium, strontium, and iodine in water-saturated cement. *Nuclear Technology*, **81**, 100–113.

Balonis, M. and Glasser, F.P. (2009) The density of cement phases. *Cement and Concrete Research*, **39**, 733–739.

Baquerizo, L.G., Matschei, T., Scrivener, K.L., Saeidpour, M. and Wadsö, L. (2015) Hydration states of AFm cement phases. *Cement and Concrete Research*, **73**, 143–157.

Baur, I. and Johnson, C.A. (2003) Sorption of selenite and selenate to cement minerals. *Environmental Science & Technology*, **37**, 3442–3447.

Bildstein, O. and Claret, F. (2015) Chapter 5 – Stability of clay barriers under chemical perturbations. Pp. 155–188 in: *Natural and Engineered Clay Barriers* (C. Tournassat, C. Steefal, I. Bourg and F. Bergaya, editors). Elsevier.

Birnin-Yauri, U.A. and Glasser, F.P. (1998) Friedel's salt, $Ca_2Al(OH)_6(Cl,OH)\cdot 2H_2O$: its solid solutions and their role in chloride binding. *Cement and Concrete Research*, **28**, 1713–1723.

Blanc, P., Lassin, A., Piantone, P., Azaroual, M., Jacquemet, N., Fabbri, A. and Gaucher, E.C. (2012) Thermoddem: A geochemical database focused on low temperature water/rock interactions and waste materials. *Applied Geochemistry*, **27**, 2107–2116.

Bonhoure, I., Baur, I., Wieland, E., Johnson, C.A. and Scheidegger, A.M. (2006) Uptake of Se(IV/VI) oxyanions by hardened cement paste and cement minerals: An X-ray absorption spectroscopy study. *Cement and Concrete Research*, **36**, 91–98.

Brunauer, S., Emmett, P.H. and Teller, E. (1938) Adsorption of Gases in Multimolecular Layers. *Journal of the American Chemical Society*, **60**, 309–319.

Cama, J., Ayora, C. and Lasaga, A.C. (1999) The deviation-from-equilibrium effect on dissolution rate and on apparent variations in activation energy. *Geochimica et Cosmochimica Acta*, **63**, 2481–2486.

Cama, J., Ganor, J., Ayora, C. and Lasaga, C.A. (2000) Smectite dissolution kinetics at 80°C and pH 8.8. *Geochimica et Cosmochimica Acta*, **64**, 2701–2717.

Cornelis, G., Etschmann, B., Van Gerven, T. and Vandecasteele, C. (2012) Mechanisms and modelling of antimonate leaching in hydrated cement paste suspensions. *Cement and Concrete Research*, **42**, 1307–1316.

Dai, Y., Qian, G., Cao, Y., Chi, Y., Xu, Y., Zhou, J., Liu, Q., Xu, Z.P. and Qiao, S. (2009) Effective removal and fixation of Cr(VI) from aqueous solution with Friedel's salt. *Journal of Hazardous Materials*, **170**, 1086–1092.

Dauzères, A., Le Bescop, P., Cau-Dit-Coumes, C., Brunet, F., Bourbon, X., Timonen, J., Voutilainen, M., Chomat, L. and Sardini, P. (2014) On the physico-chemical evolution of low-pH and CEM I cement pastes interacting with Callovo-Oxfordian pore water under its in situ CO_2 partial pressure. *Cement and Concrete Research*, **58**, 76–88.

Ganor, J., Mogollón, J.L. and Lasaga, A.C. (1999) Kinetics of gibbsite dissolution under low ionic strength conditions. *Geochimica et Cosmochimica Acta*, **63**, 1635–1651.

Gardner, L.R. (1970) A chemical model for the origin of gibbsite from kaolinite. *American Mineralogist*, **55**, 1380–1389.

Gaucher, E.C. and Blanc, P. (2006) Cement/clay interactions – A review: Experiments, natural analogues, and modeling. *Waste Management*, **26**, 776–788.

Goñi, S. and Guerrero, A. (2003) Accelerated carbonation of Friedel's salt in calcium aluminate cement paste. *Cement and Concrete Research*, **33**, 21–26.

Gougar, M.L.D., Scheetz, B.E. and Roy, D.M. (1996) Ettringite and C–S–H Portland cement phases for waste ion immobilization: A review. *Waste Management*, **16**, 295–303.

Hem, J.D. and Roberson, C.E. (1967) Form and stability of aluminum hydroxide complexes in dilute solution. *Geological Survey Water-Supply Paper*, 1827-A. US Department of the Interior, Washington.

Hsu, P.H. (1966) Formation of gibbsite from aging hydroxy-aluminum solutions. *Soil Science Society of America Journal*, **30**.

Iwaida, T., Nagasaki, S. and Tanaka, S. (2001) Sorption behavior of strontium onto C–S–H (calcium silicate hydrated phases). Pp. 901–904 in: *Studies in Surface Science and Catalysis* (N.O. Yasuhiro Iwasawa and K. Hironobu, editors). Elsevier.

Johnson, E.A., Rudin, M.J., Steinberg, S.M. and Johnson, W.H. (2000) The sorption of selenite on various cement formulations. *Waste Management*, **20**, 509–516.

Kindness, A., Lachowski, E.E., Minocha, A.K. and Glasser, F.P. (1994) Immobilisation and fixation of molybdenum (VI) by Portland cement. *Waste Management*, **14**, 97–102.

Klinger, M. and Jäger, A. (2015) Crystallographic Tool Box (CrysTBox): automated tools for transmission electron microscopists and crystallographers. *Journal of Applied Crystallography*, **48**, 2012–2018.

Köhler, S.J., Bosbach, D. and Oelkers, E.H. (2005) Do clay mineral dissolution rates reach steady state? *Geochimica et Cosmochimica Acta*, **69**, 1997–2006.

Lasaga, A.C. (1998) *Kinetic Theory in the Earth Sciences*. Princeton University Press, Princeton, USA.

Marty, N.C.M., Tournassat, C., Burnol, A., Giffaut, E. and Gaucher, E.C. (2009) Influence of reaction kinetics and mesh refinement on the numerical modelling of concrete/clay interactions. *Journal of Hydrology*, **364**, 58–72.

Marty, N.C.M., Cama, J., Sato, T., Chino, D., Villiéras, F., Razafitianamaharavo, A., Brendlé, J., Giffaut, E., Soler, J.M., Gaucher, E.C. and Tournassat, C. (2011) Dissolution kinetics of synthetic Na-smectite. An integrated experimental approach. *Geochimica et Cosmochimica Acta*, **75**, 5849–5864.

Marty, N.C.M., Munier, I., Gaucher, E.C., Tournassat, C., Gaboreau, S., Vong, C.Q., Giffaut, E., Cochepin, B. and Claret, F. (2014) Simulation of Cement/Clay Interactions: Feedback on the Increasing Complexity of Modelling Strategies. *Transport in Porous Media*, **104**, 385–405.

Marty, N.C.M., Bildstein, O., Blanc, P., Claret, F., Cochepin, B., Gaucher, E.C., Jacques, D., Lartigue, J.-E., Liu, S., Mayer, K.U., Meeussen, J.C.L., Munier,

I., Pointeau, I., Su, D. and Steefel, C.I. (2015*a*) Benchmarks for multicomponent reactive transport across a cement/clay interface. *Computational Geosciences*, **19**, 635–653.

Marty, N.C.M., Claret, F., Lassin, A., Tremosa, J., Blanc, P., Madé, B., Giffaut, E., Cochepin, B. and Tournassat, C. (2015*b*) A database of dissolution and precipitation rates for clay-rocks minerals. *Applied Geochemistry*, **55**, 108–118.

Marty, N.C.M., Grangeon, S., Warmont, F. and Lerouge, C. (2015*c*) Alteration of nanocrystalline calcium silicate hydrate (C–S–H) at pH 9.2 and room temperature: a combined mineralogical and chemical study. *Mineralogical Magazine*, **79**, 437–458.

Matschei, T., Lothenbach, B. and Glasser, F.P. (2007) The AFm phase in Portland cement. *Cement and Concrete Research*, **37**, 118–130.

Merlet, C. (1994) An accurate computer correction program for quantitative electron probe microanalysis. *Mikrochimica Acta*, **114–115**, 363–376.

Metz, V. and Ganor, J. (2001) Stirring effect on kaolinite dissolution rate. *Geochimica et Cosmochimica Acta*, **65**, 3475–3490.

Miller, W., Alexander, R., Chapman, N., Mckinlely, I. and Smellie, J. (2000) Chapter 4: Analogues of repository materials. Pp. 65–152 in: *Geological Disposal of Radioactive Waste and Natural Analogues Lessons from Nature and Archaeology* (W. Miller, R. Alexander, N. Chapman and I. Mckinlely, editors). Waste Management Series, **2**. Elsevier.

Moulin, I., Stone, W.E.E., Sanz, J., Bottero, J.Y., Mosnier, F. and Haehnel, C. (2000) Retention of zinc and chromium ions by different phases of hydrated calcium aluminate: A solid-state ^{27}Al NMR study. *Journal of Physical Chemistry B*, **104**, 9230–9238.

Parkhurst, D.L. and Appelo, C.A.J. (1999) *User's Guide to PHREEQC (version 2): A computer program for speciation, batch-reaction, one-dimensional transport, and inverse geochemical calculations*. US Geological Survey Water Resources Investigations Report 99-4259. U.S. Geological Survey, Denver, Colorado, USA, 312 pp.

Pointeau, I., Coreau, N. and Reiller, P.E. (2008) Uptake of anionic radionuclides onto degraded cement pastes and competing effect of organic ligands. *Radiochimica Acta*, **96**, 367–374.

Pollmann, H., Stefan, S. and Stern, E. (2006) Synthesis, characterization and reaction behaviour of lamellar AFm phases with aliphatic sulfonate-anions. *Cement and Concrete Research*, **36**, 2039–2048.

Qiu, X., Sasaki, K., Takaki, Y., Hirajima, T., Ideta, K. and Miyawaki, J. (2015) Mechanism of boron uptake by hydrocalumite calcined at different temperatures. *Journal of Hazardous Materials*, **287**, 268–277.

Rapin, J.P., Renaudin, G., Elkaim, E. and Francois, M. (2002) Structural transition of Friedel's salt $3CaO{\cdot}Al_2O_3{\cdot}CaCl_2{\cdot}10H_2O$ studied by synchrotron powder diffraction. *Cement and Concrete Research*, **32**, 513–519.

Renaudin, G., Kubel, F., Rivera, J.P. and Francois, M. (1999) Structural phase transition and high temperature phase structure of Friedels salt, $3CaO{\cdot}Al_2O_3{\cdot}CaCl_2{\cdot}10H_2O$. *Cement and Concrete Research*, **29**, 1937–1942.

Segni, R., Vieille, L., Leroux, F. and Taviot-Guého, C. (2006) Hydrocalumite-type materials: 1. Interest in hazardous waste immobilization. *Journal of Physics and Chemistry of Solids*, **67**, 1037–1042.

Shi, Z., Lothenbach, B., Geiker, M.R., Kaufmann, J., Leemann, A., Ferreiro, S. and Skibsted, J. (2016) Experimental studies and thermodynamic modeling of the carbonation of Portland cement, metakaolin and limestone mortars. *Cement and Concrete Research*, **88**, 60–72.

Tits, J., Geipel, G., Macé, N., Eilzer, M. and Wieland, E. (2011) Determination of uranium(VI) sorbed species in calcium silicate hydrate phases: A laser-induced luminescence spectroscopy and batch sorption study. *Journal of Colloid and Interface Science*, **359**, 248–256.

Trapote-Barreira, A., Cama, J. and Soler, J.M. (2014) Dissolution kinetics of C–S–H gel: Flow-through experiments. *Physics and Chemistry of the Earth, Parts A/B/C*, **70–71**, 17–31.

Van Es, E., Hinchliff, J., Felipe-Sotelo, M., Milodowski, A.E., Field, L.P., Evans, N.D.M. and Read, D. (2015) Retention of chlorine-36 by a cementitious backfill. *Mineralogical Magazine*, **79**, 1297–1305.